Nanoscale

Three-Dimensional Electroactive ZnO Nanomesh Directly Derived from Hierarchically Self-Assembled Block Copolymer Thin Films

Journal:	*Nanoscale*
Manuscript ID	NR-ART-01-2019-000206.R2
Article Type:	Paper
Date Submitted by the Author:	08-Apr-2019
Complete List of Authors:	Subramanian, Ashwanth ; Stony Brook University, Materials Science and Chemical Engineering Doerk, Gregory; Brookhaven National Laboratory, Center for Functional Nanomaterials Kisslinger, Kim; Brookhaven National Laboratory, Center for Functional Nanomaterials Yi, Daniel; Stony Brook University, Chemistry Grubbs, Robert B.; Stony Brook University, Chemistry; Brookhaven National Laboratory, Center for Functional Nanomaterials Nam, Chang-Yong; Brookhaven National Laboratory, Center for Functional Nanomaterials

Nanoscale

Paper

Three-Dimensional Electroactive ZnO Nanomesh Directly Derived from Hierarchically Self-Assembled Block Copolymer Thin Films

Received 00th January 20xx,
Accepted 00th January 20xx

DOI: 10.1039/x0xx00000x

www.rsc.org/

Ashwanth Subramanian, [a] Gregory Doerk, [b] Kim Kisslinger, [b] Daniel H. Yi, [c] Robert B. Grubbs, [c] and Chang-Yong Nam *[a, b]

Three-dimensional (3D) nanoarchitectures can offer enhanced material properties, such as large surface areas that amplify the structures' interaction with environments making them useful for various sensing applications. Self-assembled block copolymers (BCPs) can readily generate various 3D nanomorphologies, but their conversion to useful inorganic materials remains one of the critical challenges against the practical application of self-assembled BCPs. This work reports the vapor-phase infiltration synthesis of optoelectrically active, 3D ZnO nanomesh architectures by combining hierarchical successive stacking of self-assembled, lamellar-phase polystyrene-block-poly(2-vinylpyridine) (PS-*b*-P2VP) BCP thin films and a modified block-selective vapor-phase material infiltration protocol. The 3D ZnO nanomesh exhibit optoelectrical functionality, featuring stack-layer-number-dependent electrical conductance resembling the percolative transport originating from the intrinsic morphological network connectivity of lamellar BCP pattern with symmetric block ratio. The results not only illustrate the first demonstration of electrical functionality based on the ZnO nanoarchitecture directly generated by the infiltration synthesis in self-assembled BCP thin films but also present a new, large-area scalable, metal oxide thin film nanoarchitecture fabrication method utilizing industry-compatible polymer solution coating and atomic layer deposition. Given the large surface area, three-dimensional porosity, and readily scalable fabrication procedures, the generated ZnO nanomesh promises potential applications as an efficient active medium in chemical and optical sensors.

1 Introduction

Infiltration synthesis is a material hybridization technique derived from atomic layer deposition (ALD) during which vapor-phase organometallic precursors infiltrate and react within polymer templates. The process not only generates organic-inorganic nanocomposite hybrids with uniquely enhanced material properties but also enables a new inorganic nanopatterning methodology once the polymer matrix is selectively removed.[1-9] Different variations of the infiltration synthesis technique have been reported so far depending on precursor exposure protocols, including multi-pulse vapor phase infiltration (MPI),[10, 11] sequential infiltration synthesis (SIS),[1-9] and sequential vapor infiltration (SVI).[12, 13] These processes have been applied to polymer fibers and self-assembled block copolymer (BCP) thin film systems and have proven useful in improving various polymer properties, such as etch resistance,[5, 6, 8] triboelectric properties,[14, 15] mechanical strength,[16, 17]oil sorption ability,[18] and hydrophobic[19, 20] and hydrophilic properties,[13] antireflective properties,[21, 22] and optical properties.[23, 24] Meanwhile, patterning metal oxide films and nanoscale structures is crucial for various applications, but the development of direct metal oxide nanopatterning techniques that are low cost and easily scalable remains a challenge, especially in view of achieving high fabrication rate and device integration density.[27] Infiltration synthesis, along with other infiltration techniques such as those based on liquid-phase precursor infiltration,[25, 26] has been previously utilized for patterning metal oxide nanostructures using self-assembled BCP thin film templates[1, 2, 4] and have shown potential as an alternative to the conventional nanofabrication techniques.

BCP thin films, upon self-assembly, spontaneously generate various nanopatterns, providing various advantages for material patterning, including reduced material and processing cost, easy processing, nanoscale feature size not readily achievable by lithographic patterning, and large-scale manufacturing feasibility.[28-33] Extensive research has been carried out in the past to control the BCP self-assembly process to obtain the desired nanopatterns, and their conversion to inorganic nanopatterns by infiltration synthesis has been demonstrated, especially in the case of self-assembled poly(styrene)-*block*-poly(methyl methacrylate) (PS-*b*-PMMA) BCP thin films infiltrated by the organometallic

[a] *Department of Materials Science and Chemical Engineering, Stony Brook University, Stony Brook, New York 11794, USA.*
[b] *Center for Functional Nanomaterials, Brookhaven National Laboratory, Upton, New York 11973, USA.*
[c] *Department of Chemistry, Stony Brook University, Stony Brook, New York, 11974, USA.*

† Footnotes relating to the title and/or authors should appear here.
Electronic Supplementary Information (ESI) available: [details of any supplementary information available should be included here]. See DOI: 10.1039/x0xx00000x

precursor trimethylaluminum (TMA) (**Scheme 1**a),[33] for patterning aluminum oxide (AlO_x) nanostructures. PS-*b*-PMMA features well-established polymer synthesis and processing protocols, versatile self-assembled morphology control suitable for obtaining nanowire and nanodot structures,[34] and useful etch selectivity between PMMA and PS blocks.[35] The infiltration synthesis of AlO_x into PS-*b*-PMMA is initiated through a selective reaction between TMA and carbonyl groups in PMMA blocks—TMA, a strong Lewis acid,[36] reacts with Lewis-basic C=O (ester) groups present in PMMA during the first half cycle of infiltration process to form a bound complex (C=O···Al-$(CH_3)_2$), and the water vapor infiltrated in the following half cycle reacts with available methyl groups to form -O-Al-OH species, where the hydroxyl groups act as nucleation and growth sites for AlO_x in the subsequent infiltration cycles to finally form infiltrated AlO_x molecular network (i.e., O-Al-O-Al-O-Al-…-OH) within the PMMA block.[1, 37, 38] The resulting hybrid PS-*b*-PMMA with PMMA selectively infiltrated with AlO_x then can be directly converted to nanopatterned AlO_x inheriting the starting PMMA domain morphology once the organic polymer matrix is removed by oxygen plasma etching (**Scheme 1b**). Various AlO_x nanopatterns such as vertical lamella, vertical cylinders, and inverse cylinders (holes), and unique bilayer combinations of these structures have been patterned using the infiltration synthesis of AlO_x into PS-*b*-PMMA templates.[39]

While the AlO_x infiltration synthesis into BCP and other polymers has been extensively studied for understanding and controlling the infiltration process, the infiltration synthesis of more electroactive materials such as zinc oxide (ZnO) can have more diverse applications. Nanostructured ZnO has long been utilized for various applications including but not limited to strain sensors,[40] nanogenerators,[41] ultraviolet (UV) shields,[42] gas sensors,[43] field-effect transistors,[44] photodetectors,[45] actuators,[46] and photo-catalysts.[47] Electrically functional ZnO can be infiltration-synthesized by using diethyl zinc (DEZ) (**Scheme 1a**) and water vapor as precursors.[7, 48] For attempting ZnO infiltration synthesis into PS-*b*-PMMA templates, one may expect the Lewis-acidic DEZ to interact with the Lewis-basic groups in PMMA (e.g., C=O and ester groups), facilitating the growth of ZnO within PMMA.[1, 2, 4] However, DEZ has been known to interact poorly with PMMA and is not suitable for the *direct* infiltration synthesis of ZnO unless the PMMA domain is pre-infiltrated with AlO_x (i.e., AlO_x priming);[2, 4] seeding the PMMA block with a few cycles of AlO_x infiltration synthesis creates reactive sites (e.g., -Al-CH_3, -Al-OH) within PMMA which can catalyze the subsequent infiltration synthesis of other materials.[2] However, when growing an electroactive material such as ZnO, the amount of pre-infiltrated insulting AlO_x can in principle significantly influence the electrical properties of the finally obtained ZnO as known in Al-doped ZnO.[51] One alternative approach that enables the ZnO infiltration synthesis without AlO_x priming is chemically modifying PS-*b*-PMMA templates by UV oxidation to increase the Lewis basicity of PS (not PMMA) and therefore its interaction with DEZ, enabling the infiltration synthesis ZnO in PS domains, as we have demonstrated previously.[4] Intentional swelling of active BCP domains has been shown to enhance the amount of AlO_x infiltration synthesis,[49, 50] and may have utility to the ZnO infiltration, but no study is available. Overall, the direct infiltration synthesis of ZnO in self-assembled BCP templates without relying on either AlO_x priming or chemical modification has been rarely demonstrated so far. Furthermore, while electrical characterization has been performed on WO_3[52] and Pt[53, 54] nanowires patterned by liquid-phase infiltration in BCPs, the electrical (and optoelectrical) activity of ZnO nanostructures directly infiltration-synthesized using self-assembled BCP templates has never been reported.

Here, we report the direct, priming-free infiltration synthesis of ZnO nanostructures by combining a more chemically active, pyridine-based self-assembled PS-*b*-poly(2-vinyl pyridine) (PS-*b*-P2VP) BCP thin film template with a modified infiltration synthesis protocol called micro-dose infiltration synthesis (MDIS), enabling a higher uptake of the vapor-phase Zn precursor into the polymer template per cycle and, consequently, a high-fidelity conversion of P2VP domains into ZnO nanowire patterns without relying on AlO_x priming or chemical modification of the starting BCP templates. The structural study of as-infiltrated BCP templates and resulting ZnO nanowire patterns clearly reveals a much enhanced, uniform infiltration synthesis of ZnO within the P2VP domain via the MDIS protocol. Further demonstrated is the successive three-dimensional (3D) stacking of ZnO nanowire patterns into ZnO nanomesh structures, where respective ZnO nanowire layers are aligned orthogonally to each other, controlled by the spontaneous orthogonal alignment of self-assembled lamellar BCP template layers. The resulting 3D nanomesh structure exhibits layer-number-dependent dark and illuminated electrical conductance that resembles percolative transport behavior, reflecting the intrinsic network connectivity characteristics of the self-assembled BCP lamellar morphology and resulting individual nanowire pattern layer within the nanomesh structure. The results represent the first report of optoelectrical device functionality from metal oxide nanostructures directly generated by infiltration synthesis on self-assembled BCP templates. The modified infiltration synthesis methodology obviating AlO_x-priming or chemical modification of BCP also expands the application of BCP-based material nanopatterning towards functional device applications. The generated optoelectrically active ZnO nanomesh structure has potential as a conductometric sensor medium because of its high surface area and nanocrystallinity.

2 Results and discussion

Self-assembled PS-*b*-PMMA BCP templates have shown potential to form nanopatterns by directed self-assembly, and numerous other BCP systems have been utilized to generate self-assembled polymeric nanomorphologies, such as PS-*b*-polyisoprene (PS-*b*-PI), PS-*b*-polydimethylsiloxane (PS-*b*-PDMS), PS-*b*-poly(ethylene oxide) (PS-*b*-PEO), PS-*b*-poly(ferrocenyl dimethylsilane) (PS-*b*-PFS), and families of PS-*b*-poly(vinylpyridine) (PS-*b*-PVP).[33] Among them, PS-*b*-P2VP

(**Scheme 1a**) is one of the high χ (Flory-Huggins parameter) BCPs that has unique properties differentiated from the characteristics of more conventional PS-*b*-PMMA[55]. For instance, from the self-assembly point of view, due to the greater tendency of phase separation between PS and P2VP (represented by a larger χ) compared with that between PS and PMMA, the PS-*b*-P2VP system has a shorter critical chain length (i.e., molecular weight (M_n)) required for self-assembly than PS-*b*-PMMA, enabling smaller self-assembled domain sizes suitable for producing higher density nanopatterns.[56] Significantly, the PVP group also has an ability to coordinate with metal ligands;[57] it has been shown that the pyridine group can be complexed with metal-containing precursors, leading to the metal inclusion concentrated within the PVP domain of PS-*b*-PVP,[58-60] where PVP acts as a Lewis base (similar to the carbonyl group in PMMA) by donating the lone pair of electron present on the nitrogen atom in the pyridine ring.[61-63] This interaction has allowed the selective infiltration of aqueous metal salt ions into the PVP domains of self-assembled PS-*b*-PVP thin film templates to create nanoscale fingerprint patterns or dot structures made of gold, palladium, platinum, tungsten oxide, aluminum oxide, iron oxide, and hafnium oxide.[52, 54, 55, 57, 64-67] Recently, it has been reported that PS-*b*-PVP reverse micelle arrays can be used for the selective growth of ZnO nanodots within the PVP micelle cores by using ALD.[68] These examples suggest the potential of self-assembled PS-*b*-PVP BCP thin films as templates for the vapor-phase infiltration synthesis of electroactive metal oxide nanostructures. As we discuss below, indeed we find that the self-assembled PS-*b*-PVP thin film allows the direct, AlO_x-priming-free infiltration synthesis of ZnO nanostructures when combined with the modified infiltration synthesis protocol MDIS.

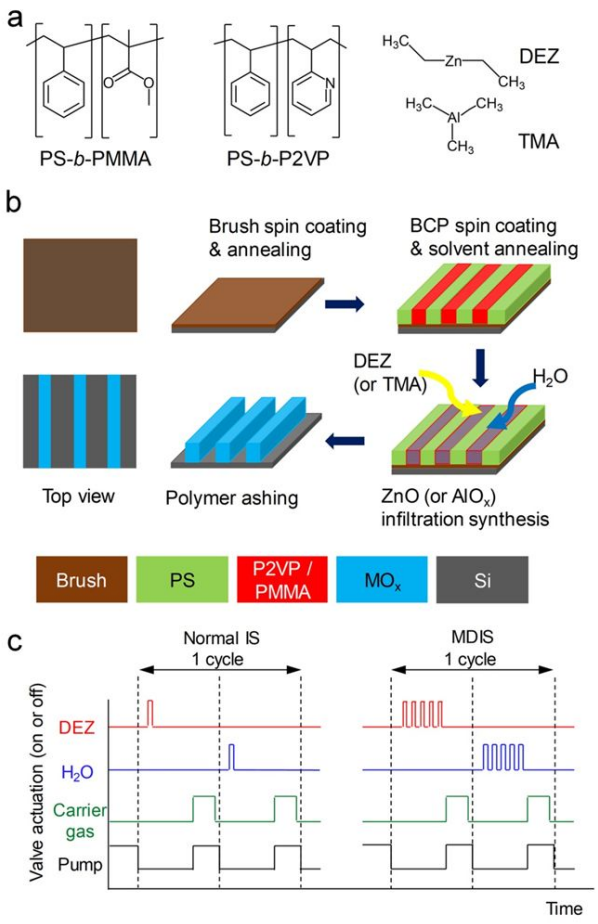

Scheme 1. (a) Nominal molecular structures of PS-*b*-PMMA, PS-*b*-P2VP, DEZ, and TMA. (b) Schematic description of the infiltration synthesis procedures for generating ZnO or AlO_x nanowire patterns using self-assembled lamellar BCP thin film templates. (c) Schematic comparison of normal infiltration synthesis (left) and MDIS (right) protocols, differentiated by the precursor dosing and purging sequences.

2.1 Comparison of Self-Assembled PS-*b*-PVP and PS-*b*-PMMA Vertical Lamellar Thin Films as ZnO Infiltration Synthesis Templates:

We first generate the self-assembled PS-*b*-P2VP thin film with vertical lamellar morphology (M_n = 50 kg/mol, 50:50 PS to P2VP molar ratio) by spin-casting the polymer solution (1 wt.% in toluene) on silicon (Si) substrates and solvent-annealing for 30 min under acetone vapor at room temperature (~22 °C).[69] To promote the perpendicular orientation of the domains, the starting Si substrate is treated with a random copolymer composed of PS and P2VP (PS-*r*-P2VP) brush layer prior to the application of PS-*b*-P2VP.[56] The thickness of resulting self-assembled PS-*b*-P2VP thin films is ~35 nm with the lamellar domain width of ~27 nm. Additionally, the control self-assembled lamellar BCP template made of PS-*b*-PMMA (M_n = 36 kg/mol 50:50 PS to PMMA ratio with the film thickness of ~35 nm and lamellar domain width of ~28 nm) is prepared separately by spin-casting 2 wt.% polymer solution (in propylene glycol methyl ether acetate (PGMEA)) on Si substrates treated by a random copolymer composed of PS and PMMA (PS-*r*-PMMA) brush and thermally annealing at 250 °C for 5 min in a nitrogen (N_2) environment.

The comparative infiltration synthesis experiment examining the influences of the types of starting BCP template and infiltration protocol clearly shows that P2VP has a higher reactivity towards infiltrating DEZ than PMMA, allowing a greater extent of domain-selective material loading without any AlO_x-priming, especially, when combined with the MDIS protocol. This ultimately enables a high-fidelity, direct BCP pattern conversion to the ZnO nanowire fingerprint pattern once removing the polymer matrix by oxygen plasma (20 W; 100 mTorr; 5 min). When first attempting to infiltration-synthesize ZnO in both the PS-*b*-P2VP and PS-*b*-PMMA films by applying eight cycles of *normal* infiltration synthesis process (**Scheme 1c**, left panel), where each cycle consists of the sequential exposures of DEZ (chamber pressure, P_c, = 2.75 Torr for 6 min) and water vapor (P_c = 280 Torr for 6 min) under the static vacuum separated by 2 min N_2 purging, the BCP pattern only converts to random ZnO nanoparticles with barely discernable nanowire fingerprint pattern for the PS-*b*-PMMA template when inspected by scanning electron microscopy (SEM) (**Figure 1**a). The ZnO structure resulting from PS-*b*-P2VP,

in contrast, features a higher quantity of ZnO deposition and more distinguishable nanowire fingerprint pattern, but, with various structural defects such as superimposed random nanoparticles, pattern agglomeration, non-uniform linewidth, and random connections between nanowires (**Figure 1b**). Despite the visible structural imperfections, the results clearly show a greater reactivity of ZnO precursors with P2VP than with PMMA. Meanwhile, the normal infiltration synthesis of AlO_x by using TMA and water as precursors yields a high-fidelity conversion to uniform AlO_x nanowire patterns for both

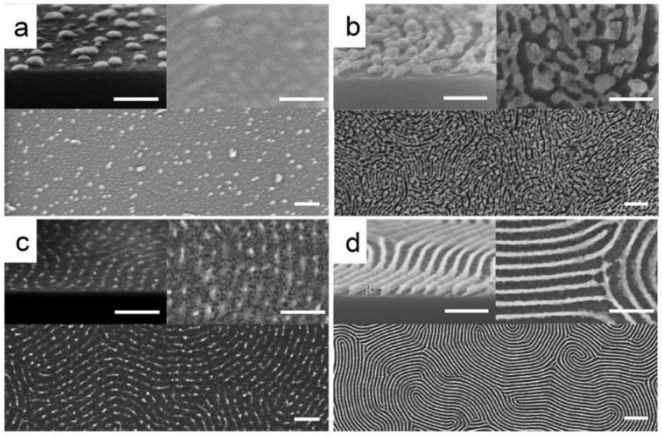

Figure 1. SEM micrographs of infiltration-synthesized ZnO structures on self-assembled lamellar PS-*b*-PMMA or PS-*b*-P2VP BCP thin films by either normal infiltration protocol or MDIS: (a) On PS-*b*-PMMA by normal protocol; (b) on PS-*b*-P2VP by normal protocol; (c) on PS-*b*-PMMA by MDIS; and (d) on PS-*b*-P2VP by MDIS. The bottom panel in each figure shows the low-magnification surface view while the top insets display the magnified views of tilted cross-section (70°, left panel) and top surface (right panel). All scale bars denote 100 nm.

PS-*b*-P2VP and PS-*b*-PMMA (**Figure S1**), indicating that the relatively inferior infiltration synthesis of ZnO originates from a lower block-selective reactivity of DEZ than TMA.

2.2 AlO_x-Priming-Free MDIS of ZnO Nanowire Fingerprint Pattern in Self-Assembled PS-b-P2VP Thin Films:

We find that the infiltration synthesis of ZnO via the MDIS protocol, in conjunction with the use of PS-*b*-P2VP as the starting BCP template, produces a uniform ZnO nanowire fingerprint pattern with its pattern conversion fidelity and resulting structural quality rivaling those of AlO_x infiltration synthesis. In the normal infiltration synthesis, the delivery (i.e., dosing or, synonymously, pulsing) of vapor-phase precursor to the chamber (by actuating the ALD valve for a period of ~10 ms) is immediately followed by an exposure period under static vacuum during which no additional precursor dosing is applied (Scheme 1c, left panel). In contrast, the MDIS protocol repeats the precursor dosing multiple times (n) with a predetermined interval (τ) during the exposure period while still maintaining the static vacuum (**Scheme 1c**, right panel), such that the total exposure time, t, by the repeated "micro-doses" is $t = n \times \tau$ for a given precursor cycle. It is noted that the previously reported SVI protocol also uses a type of multiple pulsing scheme for a given precursor, but, with intermediate N_2 purges in-between the pulses (Scheme S1).[12, 70, 71] It is noted that multiple precursor pulsing schemes have been used in *normal ALD* processes for enhanced material deposition.[72-76] Meanwhile, Ocola et al. also have indicated the use of multiple precursor pulsing during the infiltration synthesis in homopolymer thin films, but, without detailed discussion[23, 24]. To our best knowledge, no study has been reported so far, where infiltration synthesis protocols comparable to MDIS were systematically investigated using self-assembled BCP templates. When we apply 8 cycles of ZnO MDIS (with τ = 30 s, n = 12, and thus t = 6 min), the self-assembled PS-*b*-PMMA template produces an improved block-selective infiltration (**Figure 1c**) compared with the normal ZnO infiltration synthesis performed for the identical number of cycles and exposure time (**Figure 1a**), but, with still an insufficient amount of infiltration as evidenced by the mostly disconnected nanowire morphology. It is only when the MDIS is applied to the self-assembled PS-*b*-P2VP template that yields a well-structured ZnO nanowire fingerprint pattern (**Figure 1d**) with the pattern conversion fidelity and quality comparable to those of AlO_x nanowire pattern produced by infiltration synthesis (**Figure S1**).

A few factors can affect the observed dependence of the degree and quality of infiltration synthesis on the types of polymer templates and infiltrating precursors, including the higher reactivity (likely, stronger Lewis basicity) of P2VP than PMMA (due to higher Lewis basicity of pyridine group compared to ester group)[77] and higher binding affinity of TMA towards Lewis-basic groups compared to DEZ.[38, 78] Infiltration synthesis process parameters, such as exposure time, purge time, exposure pressure, and temperature, are also known to affect the fidelity and efficiency of infiltration processes in general. For instance, previous reports showed that the amount of AlO_x loading into PMMA could be varied by changing the precursor exposure time and purge time to control the residence time of the precursor within the reactor chamber for the subsequent diffusion of precursor molecules into and reaction with the polymer matrix.[37, 79]

One particular aspect of the MDIS protocol that is expected to contribute to the improved ZnO infiltration synthesis is the increased precursor concentration in the chamber compared with the normal infiltration synthesis protocol: During the DEZ exposure period of infiltration synthesis, the chamber pressure stays at 2 – 4 torr, which is much lower than the saturation vapor pressure of DEZ in the headspace of DEZ precursor cylinder (~26.7 torr at 30 °C).[80] Assuming that each actuation (i.e., opening and closing) of the ALD valve draws all the DEZ molecules available in the cylinder headspace, and the DEZ vapor acts as an ideal gas, the number of DEZ molecules introduced to the chamber during each dosing can be estimated based on the DEZ saturation vapor pressure, which is governed by the Antoine equation.[81] Compared with performing a single precursor dosing as in the normal infiltration synthesis, the micro-doses applied during the MDIS protocol should in principle gradually increase the number of DEZ molecules in the chamber available for the diffusion into the polymer matrix during the exposure period, in proportion to the number of repeated micro-doses (**Scheme 2**), which is

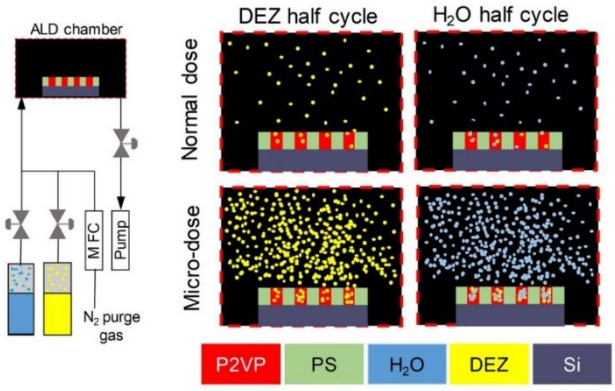

Scheme 2. Left panel: General schematic of an ALD system. MFC denotes mass flow controller. Right panel: Schematic description of ALD chamber showing the difference in the amounts of precursor molecules during the exposure period in normal infiltration (top) and MDIS (bottom) protocols.

consistent to the stepwise increase in the temporal pressure profile in the reaction chamber measured during the DEZ micro-dosing (**Figure S2**). This, in turn, will increase the probability for the reaction to take place between DEZ and P2VP, due to the increased amount of DEZ diffusing into P2VP domain, resulting in a more uniform ZnO infiltration synthesis in the polymer matrix for a given exposure time.[82]

2.3 Internal Structures of ZnO-Infiltrated Self-Assembled PS-*b*-P2VP Thin Films by MDIS:

Cross-sectional transmission electron microscopy (TEM) carried out on the as-ZnO-infiltrated self-assembled PS-*b*-P2VP thin film templates not only confirms the superior amount of ZnO infiltration but also reveals a much more uniform block-selective infiltration enabled by the MDIS protocol (**Figure 2**). The bright-field TEM micrographs (**Figure 2a** and **2b**) clearly show two major differences between the normal infiltration synthesis and MDIS. While both the normal infiltration and MDIS show a block-selective infiltration with the spatial distribution of infiltrated ZnO closely resembling one of the two domains (i.e., P2VP) of the nominal, vertical lamellar morphology of self-assembled PS-*b*-P2VP thin film, the ZnO infiltration via the normal infiltration synthesis is mainly concentrated at the top surface of the infiltrated polymer domain as revealed by the dark top region stemming from the higher atomic number of Zn than that of carbon, the predominant element of polymer matrix (**Figure 2a**). The bulk of the domain below the dark top region also shows a sign of some degree of ZnO infiltration considering its darker contrast than those of the neighboring un-infiltrated polymer domains or top carbon capping layer deposited after the infiltration synthesis for TEM sample preparation.

In stark contrast, the MDIS protocol yields a much more uniform, higher-quantity infiltration of ZnO throughout the given domain with the absence of the concentrated top layer (**Figure** 2b) as the whole infiltrated domain features a uniform dark contrast. This is consistent with the observed high-fidelity ZnO nanowire fingerprint pattern obtained by MDIS after ashing the polymer matrix (**Figure 1d**). The high-angle annular dark-field (HAADF) imaging and associated energy dispersive spectroscopy (EDS) elemental mapping performed by scanning TEM clearly confirm that the uniform, block-selectively infiltrated material within the domain is ZnO (**Figure 2c**). It is noted that the thickness of as-infiltrated PS-*b*-P2VP is ~45 nm for both the normal infiltration synthesis and MDIS, comparable to the nominal thickness of starting self-assembled PS-*b*-P2VP thin film. Both protocols also result in the width of the ZnO-infiltrated domain of ~18 nm, ~35 % larger than that of the un-infiltrated domain (~ 13.5 nm), indicating either the infiltration-induced volume expansion of P2VP domain or the infiltration synthesis spilled over the P2VP domain into the PS domain. Meanwhile, both bright-field and dark-field TEM micrographs and EDS mapping reveal the presence of thin ZnO bottom layer (<10 nm) underneath the infiltrated self-assembled PS-*b*-P2VP film, which is likely caused by the infiltration synthesis of ZnO in the PS-*r*-P2VP brush layer.

2.4 Generation of Multi-Layered ZnO Nanomesh Structures:

We combine the ZnO MDIS in PS-*b*-P2VP and the spontaneous orthogonal self-aligning of successively stacked self-assembled lamellar BCP thin films to generate a multi-layered ZnO nanomesh structure. Although complex monolayer patterns based on the BCP self-assembly have been well documented,[33] extending the patterning control to build multi-layered 3D BCP structures is a promising route for

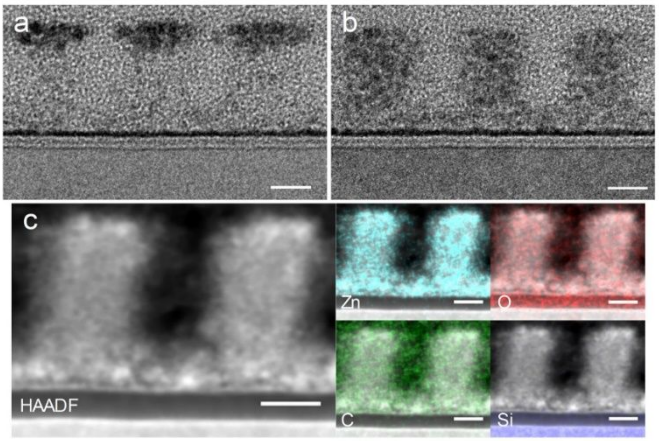

Figure 2. Bright-field cross-sectional TEM micrographs of the self-assembled PS-*b*-P2VP vertical lamellar thin films immediately after ZnO infiltration synthesis (as-infiltrated) by (a) normal infiltration protocol and (b) MDIS. (c) HAADF STEM micrograph (left panel) and associated EDS areal elemental mappings (right panel; Zn, O, C, and Si) obtained from the as-ZnO-infiltrated self-assembled PS-*b*-P2VP lamellar thin film cross-section. All scale bars denote 10 nm.

generating complex, 3D inorganic structures useful for electronic device applications if the 3D polymer template can be converted to electrically functional inorganic materials. Previous reports have shown that the BCP self-assembly can be tuned to generate 3D nanomesh structures via the orthogonal self-alignment of successively stacked self-assembled BCP layers over either lithographically patterned trenches[83] or self-assembled BCP bottom layer templates.[39, 83-

[85] Such spontaneous orthogonal alignment has been attributed to the entropic energy penalty incurred by the polymer chain stretching or compression when lamellar BCP domains align parallel with the underlying corrugation.[84, 86-89] Nevertheless, the pattern transfer or direct conversion of these self-assembled 3D organic polymer nanostructures into more electrically functional *inorganic* materials has been rarely reported due to intrinsic challenges in the pattern transfer or conversion.

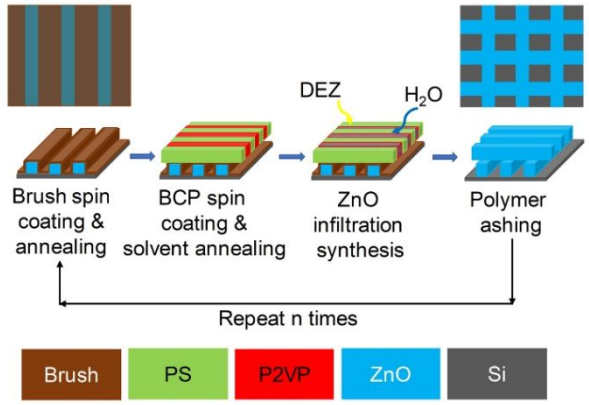

Scheme 3. Schematic description of ZnO nanomesh structure fabrication procedures.

Only recently, Majewski and Yager et al. demonstrated the construction of multi-layered inorganic nanomesh structures made of noble metals and oxides by using the aqueous and vapor-phase infiltration in the photothermally annealed, shear-aligned cylindrical-phase PS-*b*-P2VP BCP thin film templates,[53] where up to three layers of inorganic nanowire arrays could be successively stacked to generate the nanomesh structures with controlled pattern symmetries. However, the proper laser-based photothermal BCP pattern alignment must rely on rather complicated engineering of thermal absorption and shear-inducing layers, whose application in the large-area device fabrication can be challenging.

In view of producing ZnO nanomesh structures suitable as active sensing media, the large surface areas and electrical continuity between layers are desirable, but the stringent inter-layer alignment is not critical. Thus, we instead utilize the spontaneous orthogonal self-alignment of successively stacked lamellar BCP patterns.[88, 89] Despite the less perfect alignment compared with the directed self-assembly processes based on photothermal laser annealing or top-down, lithographically fabricated physical templates,[83, 86, 87] the spontaneous orthogonal alignment scheme not only is much simpler to apply to a large area without using specially engineered substrates or complicated pre-processing but also enables inter-layer electrical connections across the stacked ZnO nanomesh layers as shown later.

The fabrication of ZnO nanomesh first starts with generating a monolayer of ZnO nanowire fingerprint pattern on a substrate via the earlier elaborated self-assembly of lamellar-phase PS-*b*-P2VP thin film, ZnO MDIS, and polymer ashing by oxygen plasma. One additional step added before stacking the second layer is the deposition of 1 nm thick TiO_x layer by normal ALD (at 250 °C) to maintain the structural integrity of ZnO nanowires under the elevated temperature, whose critical importance is detailed in later sections. Then, another monolayer of lamellar PS-*b*-P2VP thin film is spin-cast on top of the first ZnO nanowire fingerprint pattern layer after treating it with a PS-*r*-P2VP brush layer. When the second PS-*b*-P2VP thin film is subjected to the acetone vapor annealing at room temperature (~22 °C, for 30 min), the first ZnO nanowire layer at the bottom serves as a template for the lamellar pattern in the second PS-*b*-P2VP layer to align orthogonally as the periodic surface protrusion on the bottom ZnO nanowire array poses an energetic penalty against the parallel alignment of the second lamellar BCP layer as discussed earlier.[86, 87] The self-aligned second BCP layer is then infiltrated with ZnO by the 8 cycles of MDIS, followed by the oxygen plasma ashing of polymer and rapid thermal processing (RTP) under O_2 at 600 °C for 5 min to fully consolidate the inorganic structure. The resulting two-layered ZnO nanomesh (**Figure 3**) has square shaped pores with a size of ~15 nm × ~15 nm as the ZnO nanowire array in the second layer is predominantly oriented orthogonally to the bottom first layer. This spontaneous orthogonal stacking process can be repeated multiple times (**Scheme 3**), and we were able to generate ZnO nanomesh structures consisting of up to six successively stacked ZnO nanowire layers (**Figure 4**), doubling the maximum number of inorganic or polymeric nanomesh layers the previous studies have achieved utilizing the directed photothermal or spontaneous alignment of BCP layers.[53, 83] It is noted that the maximum number of stacked ZnO nanomesh layers in the current study is limited by the structural integrity of bottom ZnO layers, which starts decreasing when too many ZnO nanomesh layers are stacked due to the ZnO grain growth and agglomeration under the repeated heat treatments as we discuss below. We address the issue by utilizing heteroatom dopants that suppress grain growth and agglomeration.

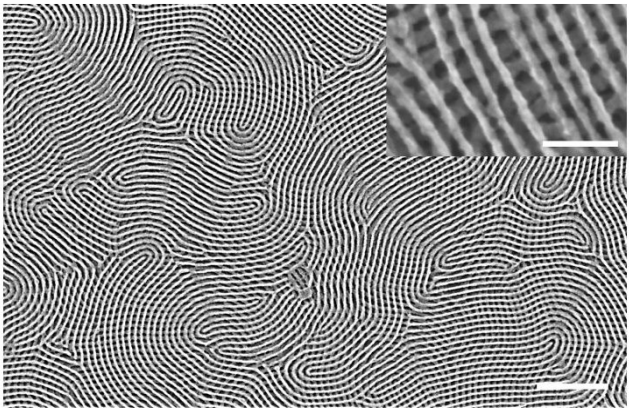

Figure 3. SEM micrographs (top view) of the two-layered ZnO nanomesh structure featuring the orthogonal self-alignment between the bottom and top ZnO nanowire pattern layers. Scale bar denotes 300 nm. The inset shows a magnified view. Scale bar denotes 100 nm.

2.5 Improved Thermal Stability of as-Infiltration-Synthesized ZnO Nanowire Fingerprint Patterns by Ultrathin TiO_2 Capping Layers:

Generally, ZnO can be thermally annealed to improve its properties for functional applications,[90] such as structural quality (e.g., crystallinity and lattice strain),[91] optical properties (e.g., improved UV luminescence),[92] and charge transport characteristics (e.g., electron mobility).[44] The oxygen plasma ashing of organic matrix applied to the as-ZnO-infiltrated polymer hybrid typically leaves behind residual carbon atoms in the resulting ZnO nanostructure, and the complete removal of these carbon impurities from ZnO to ensure suitable electrical properties for device applications requires an additional thermal annealing, such as O_2 RTP,[44] during which the removal of carbon atoms, along with the consolidation of ZnO grains and the potential carbothermal reduction of ZnO (i.e., oxygen vacancy/charge carrier generation), can activate the electrical conduction.[93] However, one challenging issue of applying the thermal treatment on the infiltration-synthesized ZnO is the degradation of nanowire morphology due to excessive grain growth and granularization: When a monolayer

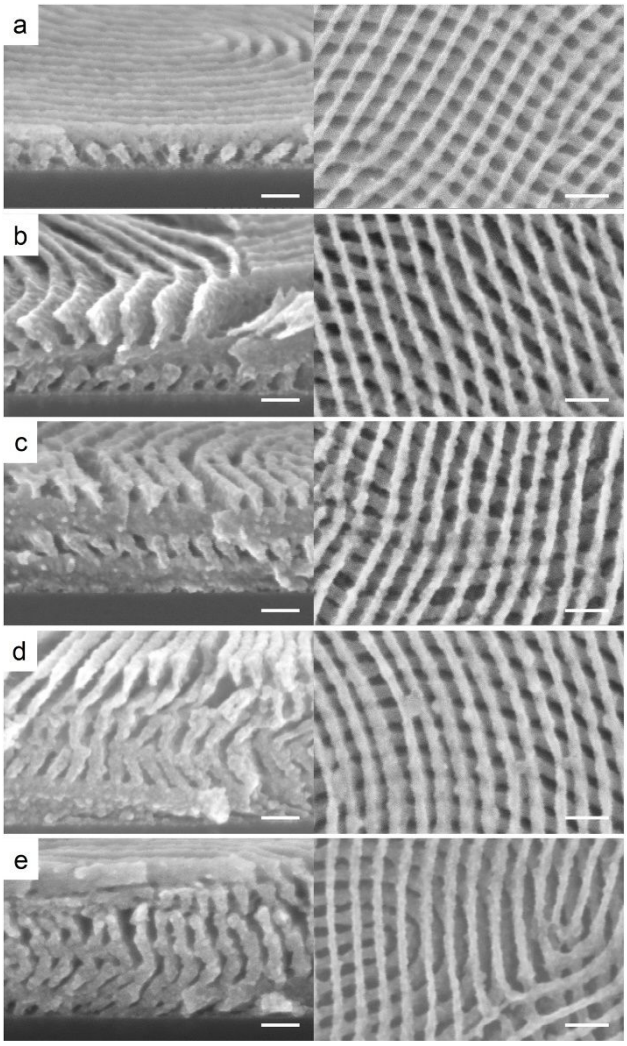

Figure 4. Cross-sectional (left column) and top-view (right column) SEM micrographs of ZnO nanomesh structures with varying number of stacked ZnO nanowire pattern layers: (a) 2, (b) 3, (c) 4, (d) 5, and (e) 6 layers. All scale bars denote 100 nm.

of ZnO nanowire fingerprint structure obtained by ashing the polymer matrix of ZnO-infiltrated PS-*b*-P2VP lamellar pattern is

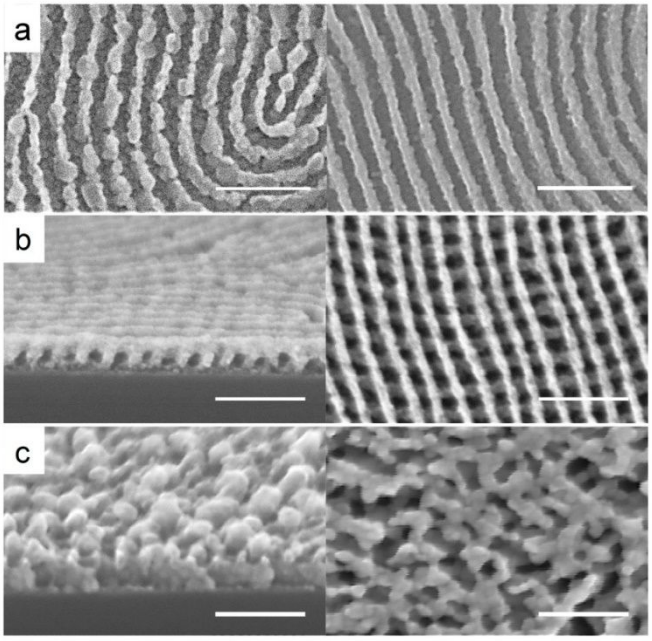

Figure 5. SEM micrographs featuring the effect of 1 nm TiO_2 conformal coating on the thermal stability of infiltration-synthesized ZnO morphology after 600 °C RTP. (a) ZnO nanowire patterns without (left panel) and with (right panel) TiO_2 conformal coating. (b) Two-layered ZnO nanomesh structures: (b) With TiO_2 coating and (c) without TiO_2 coating (left panel: 70°-tilted cross-section; right panel: Top view). All scale bars denote 100 nm.

subjected to the O_2 RTP at 600 °C for 5 min, the nanowire morphology, though not fully disconnected, becomes significantly granular along the wire axis, with the development of crystal facets (**Figure 5**a, **left panel**), similar to the grain agglomeration and growth previously observed for ZnO films annealed at high temperatures.[94] The observed granularization is most likely caused by the highly nanocrystalline (with grain size <~5 nm) internal structure of as-infiltration-synthesized ZnO nanowires[44] that is naturally prone to the grain growth under elevated temperatures, as well as the substantial ionic bonding nature of ZnO [95] that generally favors facetted grain growth. Since the thermal treatment is repeated for every stacked ZnO nanomesh layer, the thermal stability issue becomes significantly exacerbated, rendering the layer stacking, in fact, impossible as discussed below.

We discover a dramatic increase in the thermal stability of ZnO nanomesh layers by the application of 1 nm thick TiO_x capping layer via normal ALD before the thermal treatment. This enables the successive stacking of ZnO nanowire fingerprint patterns and, consequently, structurally intact, electrically active multi-layered ZnO nanomesh structures. Previous studies have shown that the grain growth in ZnO thin films can be regulated and suppressed by using nano-coatings[96] or doping of amorphous materials, such as AlO_x[97] and TiO_x,[98-100] using ALD. Such secondary phases, when introduced into the microstructure of nanomaterial as heterogenous surface oxides or dopant atoms on the nanomaterial, attach to the moving grain boundaries, acting as additional diffusion barriers by imposing a retarding force greater than the driving force for grain boundary diffusion,

thus preventing crystal growth (Zener pinning effect).[101] When we apply a similar strategy by capping the as-infiltration-synthesized ZnO nanowire layer with 1 nm-thick TiO_2 layer via normal ALD, the improved thermal stability of infiltration-synthesized ZnO structure is indeed immediately apparent: The monolayer ZnO nanowire fingerprint pattern, coated with 1 nm-thick conformal TiO_2 layer, does not show any sign of granularization after the 600 °C O_2 RTP (**Figure 5a, right panel**), maintaining the initial nanowire morphology obtained by the oxygen plasma ashing of polymer matrix (**Figure 1d**). More significantly, this achieved thermal stability becomes one of the key factors that enable the successive stacking of ZnO nanowire layer to eventually generate the electroactive ZnO

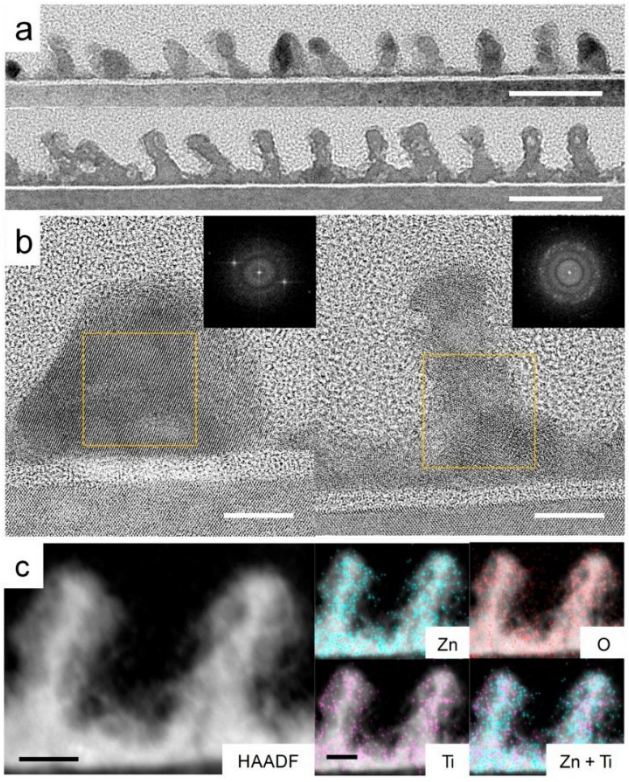

Figure 6. Cross-sectional TEM and STEM micrographs showing the effect of 1 nm TiO_2 conformal coating on the internal structure of infiltration-synthesized ZnO nanowire pattern after 600 °C RTP. (a) Low-magnification bright-field TEM images: Without TiO_2 coating (top panel) and with TiO_2 coating (bottom panel). Scale bars denote 50 nm. (b) High-resolution bright-field TEM images with insets showing FFT of yellow-squared areas: Without TiO_2 coating (left panel) and with TiO_2 coating (right panel). Scale bars denote 10 nm. (c) HAADF STEM image (left panel) and associated EDS areal elemental mappings (right panel; Zn, O, Ti): With TiO_2 coating. Scale bars denote 10 nm.

nanomesh structure: As shown in **Figure 5b**, the two-layered ZnO nanomesh structure with the TiO_2 conformal coating features a fully intact nanomesh structure even after O_2 RTP treatment at 600 °C for 5 min, which is in a drastic contrast to the complete disintegration of two-layered ZnO nanomesh structure after the same O_2 RTP treatment if the ultrathin TiO_2 conformal coating is not applied (**Figure 5c**).

The cross-sectional TEM, interrogating the internal grain

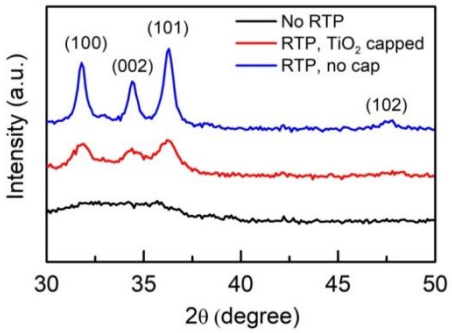

Figure7. Thin film XRD spectra obtained from ZnO nanowire pattern layers. From bottom to top: As-infiltration-synthesized with no RTP applied (black line); with 1 nm TiO_2 conformal coating (TiO_2 capped) after 600 °C RTP (red line); and without TiO_2 coating after 600 °C RTP (blue line). Diffraction peaks are labeled with corresponding ZnO crystal planes.

structures of the thermally annealed monolayer ZnO nanowire fingerprint pattern layer, clearly shows the suppression of grain growth and granularization by the application of 1 nm-thick TiO_2 capping layer. The low-magnification TEM micrograph (**Figure 6**a, top panel) reveals more rounded granular cross-sectional morphology in the ZnO nanowire sample without the TiO_2 capping layer, with the uneven image contrast of individual grains within the cross-section. With the TiO_2 capping layer, the ZnO nanowire now features square-shaped cross-sections (**Figure 6a, bottom panel**), largely resembling the vertical lamellar domain morphology of the starting self-assembled BCP thin film template (**Figure 2b**), while showing relatively more even contrast in the cross-section without discernable individual crystal grains. Beside the apparent difference in cross-sectional morphology, the two dissimilar image contrasts suggest the existence of much larger crystalline grains in the ZnO sample without the capping layer, considering that the uniformly dark regions in a given cross-section represent large single grains oriented along the TEM zone-axis (i.e., diffraction contrast). Indeed, the high-resolution TEM and fast Fourier-transform (FFT) of individual cross-sections show that the ZnO nanowire without the TiO_2 capping displays only a few grains in a given cross-section (**Figure 6b, left panel**), in contrast to the highly nanocrystalline grains in the counterpart with the TiO_2 capping layer (**Figure 6b, right panel**). Thin-film X-ray diffraction (XRD) performed on larger areas also consistently confirms the suppressed grain growth and the resulting nanocrystallinity in the TiO_2-capped ZnO nanowire (**Figure 7**); prior to the O_2 RTP, the as-infiltration-synthesized ZnO nanowire fingerprint pattern features no diffraction peaks other than a broad background, indicative of a largely amorphous structure. The 600 °C RTP induces crystallization as evidenced by the emergence of diffraction peaks consistent with the hexagonal wurtzite ZnO phase, but, much more pronouncedly for the ZnO nanowire sample without the TiO_2 capping layer, with the corresponding average grain size of ~16 nm (obtained by the Scherrer analysis [102]), compared with ~7 nm of the ZnO nanowire with TiO_2 capping layer (Table S1), again confirming the suppression of

ZnO grain growth by the capping layer. The cross-sectional EDS mapping of TiO_2-capped ZnO nanowire performed by scanning TEM shows that Ti is distributed evenly through the nanowire cross-section after the 600 °C RTP (**Figure 6c**), suggesting the diffusion of Ti atoms from the TiO_2 conformal ALD coating into the ZnO matrix and likely their interference with Zn atom diffusion and associated ZnO grain growth. Ti has been studied as a dopant for improving the electron mobility of ZnO,[103] considering their similar ionic radii (cf., Ti^{4+}: 0.068 nm and Zn^{2+}: 0.074 nm) that can permit the substitutional replacement of Zn by Ti in the wurtzite ZnO structure.[104] At low Ti dopant concentration, Ti atoms are also known to be present at interstitial sites, creating new grain boundaries, acting as diffusion barriers under the thermal processing and leading to the reduction of ZnO crystal growth [99, 104] via the aforementioned Zenner pinning effect.[101]

2.6 Electrical Functionality of ZnO Nanomesh Structures

Finally, we test the electrical functionality of the generated ZnO nanomesh structure and find a tunable electrical conductance with respect to the number of ZnO nanomesh. Two-probe ZnO nanowire mesh devices are fabricated by lithographically patterning Ti/Au (40 nm/60 nm thick) interdigitated electrodes (channel width of ~15 × 80 □m and length of 4 □m) on the ZnO nanomesh generated on SiO_2 (300 nm)/Si substrates (**Figure 8**). The representative dark current-voltage (I-V) characteristics (**Figure 9**a) largely feature a highly

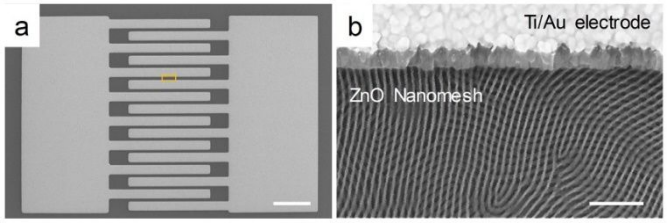

Figure 8. SEM micrographs (top view) of a fabricated ZnO nanomesh device: (a) Low-magnification image showing the Ti/Au interdigitated electrode patterned on ZnO nanomesh. Scale bar denotes 50 μm. (b) High-resolution image magnifying the electrode-nanomesh interface in the yellow rectangular area in (a). Scale bar denotes 300 nm.

resistive state showing only I = ~0.12 pA at V = 100 V for the monolayer ZnO nanowire fingerprint pattern. The two-layered and three-layered ZnO nanomeshes still show similarly high resistances with I < ~18 pA at V = 100 V. A sign of the electrical conduction onset appears in the four-layered ZnO nanomesh structure with I = ~ 85 pA at V = 100 V, and the continued increase of the number of nanomesh layers ultimately yields I = ~300 pA at V = 100 V for the six-layered ZnO nanomesh. If plotting the differential conductances obtained at low and high voltages (near V = 0 V and 100 V, respectively) with respect to the number of ZnO nanomesh layers, the conduction onset behavior is much more clearly identified (**Figure 9b and 9c**); at both low and high voltages, there exist negligible conductances up to three layers, but from four to six layers, a rapid increase in conductance is clearly visible, which seemingly resembles the conduction onset observed in percolative conduction networks, such as those in polymer-carbon nanotube composites, after the percolation threshold is reached.[105]

The notion of percolative network connectivity is in fact highly relevant to the self-assembled lamellar-phase BCP fingerprint pattern, and we reason that the observed onset behavior of electrical conduction in the multi-layered ZnO nanomesh is originating from the lack of long-range percolative conduction network in each ZnO nanowire fingerprint pattern layer. A series of reports by Stoykovich et al. have shown that the lamellar morphology in self-assembled BCP thin films can have varying network connectivity and long-range continuity depending on the compositional symmetry (i.e., block ratio) of the used BCP system.[106, 107] Especially, the symmetric, 50:50-block-ratioed lamellar fingerprint pattern (one that was used in the present study) in principle lacks the long-range network connectivity and, therefore, percolation,

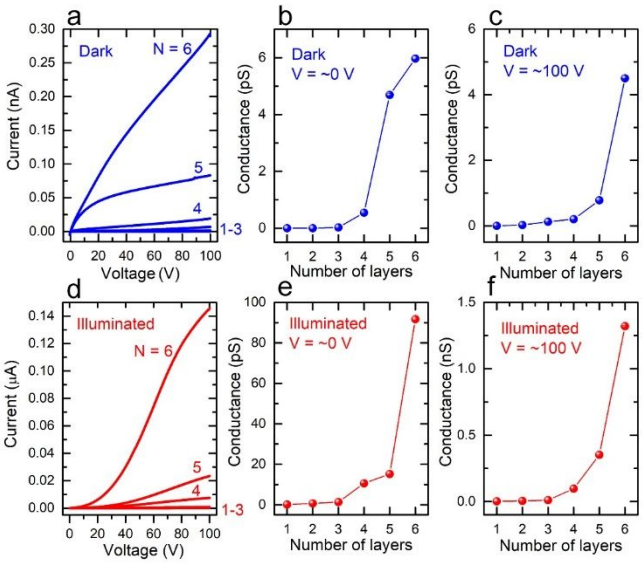

Figure 9. (a) Dark I-V characteristics of ZnO nanomesh structure with varying number of constituting ZnO nanowire pattern layers (N). Dark differential conductance of ZnO nanomesh with respect to the number of ZnO nanowire layers at: (b) V = 0 V and (c) V = 100 V. (d) Illuminated I-V characteristics of ZnO nanomesh structure with varying number of constituting ZnO nanowire pattern layers. Illuminated differential conductance of ZnO nanomesh with respect to the number of ZnO nanowire layers at: (e) V = 0 V and (f) V = 100 V.

unless a certain density of structural defects that promote inter-domain connections (e.g., branching) are present.[107] We expect that each ZnO nanowire fingerprint pattern layer that constitutes the multi-layered ZnO nanomesh structure does not have an in-plane percolative conduction network continuous throughout the device channel since the nanowire layer is directly converted from the symmetric, 50:50-block-ratioed PS-*b*-P2VP BCP system whose of degree of self-assembly was promoted by the solvent annealing, a process known to produce less structural defects in self-assembled BCPs compared with typical thermal annealing processes. [108]

The observed, negligible conductance of monolayer ZnO nanowire fingerprint pattern is consistent with the suggested lack of in-plane percolation. The successive orthogonal

stacking of nanowire fingerprint pattern layers into the multi-layered ZnO nanomesh increases the 3D network connectivity via inter-layer connections, and the eventual electrical conduction onset occurs once a complete 3D percolation through the device channel is established with enough numbers of stacked ZnO nanowire fingerprint pattern layers. The observation that both the high- and low-voltage conductances of ZnO nanomeshes have the identical threshold number of nanowire layers for the conduction onset suggests that the non-linear increase of conductance with respect to the number of constituting nanowire layers is not likely much influenced by the intrinsic charge transport characteristics of infiltration-synthesized ZnO, which features a highly resistive, carrier-depleted state originating from its reduced dimension and nanocrystallinty combined with the surface oxygen chemisorption.[48]

The layer-number-dependent I-V characteristics of ZnO nanomesh structures measured under the *optical illumination* further support that the origin of the conduction onset in the multi-layered ZnO nanomesh is from the geometrical percolation; it has been shown that the light absorption increases the background charge carrier density by not only directly exciting photo-carriers but also assisting the desorption of chemisorbed surface oxygens and yielding the photo-gain effect (i.e., additional mobile charge carrier generation).[48, 109] If the observed conduction onset behavior is related with the high-resistivity state in the infiltration-synthesized ZnO (i.e., intrinsic material property), the alleviation of high resistance by photo-excitation should in principle change the layer-number-dependent I-V characteristics. The measured data under illumination, however, clearly exhibit a nearly identical layer-number-dependent conductance onset as those measured in dark (**Figure 9d**); when illuminated by a microscope tungsten light (~3.5 mW), the electrical conductance is still negligible for the ZnO nanomeshes with less than three nanowire layers but rapidly increases once the number of nanowire layers is larger than four. The low- and high-voltage differential conductances again consistently exhibit the conduction onset for four or more nanowire layers (**Figure 9e and 9f**). Overall, these observations confirm that the lack of physical long-range network connectivity in each ZnO nanowire fingerprint pattern layers causes the percolative 3D charge conduction through the ZnO nanomesh structure. It is noted that the threshold number of nanowire layers for the conduction onset in ZnO nanomesh is expected to be modifiable by controlling the network connectivity in the constituting ZnO nanowire fingerprint pattern layer (e.g., use of asymmetric-block-ratioed BCP thin films).[106] We also recognize that the electrical characteristics of produced ZnO nanomesh structures may have been affected by Ti capping since Ti doping in ZnO, in general, tends to decrease the electrical conductivity of ZnO by reducing the concentration of oxygen vacancy.[110]

3 Conclusions

In summary, we have demonstrated the direct, AlO_x-priming-free infiltration synthesis of ZnO nanostructures in self-assembled BCP thin film templates by combining the PS-*b*-P2VP BCP system and the modified infiltration synthesis protocol MDIS. A combination of control experiments clearly showed the higher reactivity of pyridine block toward the weakly interacting, infiltrating Zn precursor DEZ, compared with that of the PMMA block in PS-*b*-PMMA, the prototypical BCP system being used for the vapor-phase materials infiltration. When combined with the MDIS protocol featuring the repeated multiple dosing of a given precursor under a static vacuum during the exposure period, the self-assembled PS-*b*-P2VP thin film of vertical lamellar phase could be directly converted into the ZnO nanowire fingerprint pattern with a high pattern-conversion fidelity without relying on the AlO_x-priming process generally required to infuse weakly interacting material precursors in the self-assembled BCP thin film. Also devised was the method to improve the structural stability of the ZnO nanowire pattern at elevated temperatures using a nanometer-thick conformal coating of TiO_2, allowing the full consolidation of the inorganic matrix and the removal of carbon impurities without morphology granularization, critical for activating the electrical functionality and maintaining the structural integrity in the infiltration-synthesized ZnO nanostructures. By further implementing the successive stacking of ZnO nanowire fingerprint pattern layers with the spontaneous orthogonal inter-layer alignment, the multi-layered ZnO nanomesh structure has been created, where the geometrical network connectivity in each constituting ZnO nanowire fingerprint layer controlled the overall percolative charge conduction through the 3D ZnO nanowire nanomesh structure, causing the layer-number-dependent onset of current conduction behavior. The identified high block-selective reactivity of the pyridine-based BCP system and the developed MDIS protocol expand the applicability of vapor-phase material infiltration based on self-assembled BCP thin film templates toward generating functional inorganic nanostructures. The demonstrated electroactive ZnO nanomesh structure, for instance, has potential applications as active media in chemical and optical sensing devices given the useful tunability of nanostructural characteristics and the low-cost large-area scalability enabled by the solution processing of polymer templates and the ALD-based low-temperature vapor-phase material infiltration.

4 Materials and method

4.1 Materials: PS-*b*-P2VP (M_n = 50 kg/mol; 50:50 block ratio) and PS-*b*-PMMA (M_n = 36 kg/mol; 50:50 block ratio) were purchased from Polymer Source, and PS-*r*-PMMA (M_n = 9.2 kg/mol; 61:39 block ratio) was provided by The Dow Chemical Company. The PS-*r*-P2VP (M_n = ~22 kg/mol; 58% PS fraction) neutral brush was synthesized as described in the Supporting Information. PGMEA, acetone, toluene, TMA, and DEZ were purchased from Sigma-Aldrich and used as received. Photoresist S1811 and MF312 developer were procured from MicroChem and used as received.

4.2 Preparation of Self-Assembled PS-b-P2VP and PS-b-PMMA Vertical Lamellar Thin Films: Si substrates were cleaned by oxygen plasma (20 W; 100 mTorr; 1 min) (March CS-1701). The brush solution (PS-*r*-P2VP (1 wt.% in toluene) or PS-*r*-PMMA (1 wt.% in PGMEA)) was spin-cast on the cleaned Si substrate (1500 rpm; 45 s). The brush film was annealed on a N_2-blanketed hot plate (Wenesco Inc. H0909AA) at 250 °C for 5 min. Excess brush polymers not grafted to the substrate were removed by rinsing with PGMEA while spinning the sample at 3000 rpm. The lamellar-phase BCP solution (PS-*b*-P2VP or PS-*b*-PMMA; 1 wt.% in toluene and 2 wt.% in PGMEA, respectively) was then spin-cast on the brush-treated Si substrate (3000 rpm; 45 s). The resulting PS-*b*-P2VP BCP film was solvent-vapor-annealed at room temperature (22 °C) for 30 min to induce the self-assembly by placing the sample on a stage inside a cylindrical metal container (volume of ~60 ml) with 6 ml of acetone reservoir and a top glass lid through which the BCP film thickness was monitored in-situ by an interferometer (Filmetrics Inc.). The self-assembly of PS-*b*-PMMA BCP film was achieved by thermally annealing the sample on a N_2-blanketed hot plate at 250 °C for 5 min.

4.3 Infiltration Synthesis of ZnO and AlO_x: The infiltration synthesis of ZnO and AlO_x on self-assembled BCP thin film templates was carried out in a commercial ALD system (Cambridge Nanotech Savannah S100) at 85 °C using DEZ and TMA as respective metal organic precursors along with water as an oxidant. A single normal ZnO infiltration synthesis cycle by the normal protocol consists of, in sequence: Exposure of DEZ for 6 min under a static vacuum (~3 Torr); chamber purging by N_2 (100 sccm) for 2 min; exposure to water vapor for 6 min; and chamber purging by N_2 (100 sccm) for 2 min. A single AlO_x infiltration synthesis cycle by the normal protocol consists of the identical steps described above except that the precursor exposure period of 100 s (chamber pressure of ~10 Torr during TMA infiltration), instead of 6 min, was used. The MDIS of ZnO also had the precursor exposure period of 6 min, identical to that of the normal protocol, but the precursor (both DEZ and water) dosing was repeated every 30 s during the exposure period (total 12 repeated dosings). The infiltration synthesis was followed by the initial removal of organic polymer matrix by oxygen plasma ashing (20 W; 100 mTorr; 5 min; room temperature) and the further consolidation of the inorganic matrix and the removal of carbon impurities by O_2 RTP at 600 °C for 5 min (Modular Process Technology RTP-600S). For selected infiltration-synthesized ZnO nanostructure samples, a 1 nm-thick conformal TiO_2 layer was deposited via the normal ALD mode (at 250 °C; 50 cycles) by using titanium(IV) isopropoxide and water as precursors prior to the application of O_2 RTP.

4.4 ZnO Nanomesh Device Fabrication: A photoresist layer (S1811) was spin-cast on the ZnO nanomesh generated on a SiO_2 (300 nm)/Si substrate (3000 rpm; 30 s) and baked on a hot plate (100 °C; 60 s). An interdigitated electrode pattern (channel length and width of ~4 □m and ~15 × 80 □m, respectively) was exposed by using a home-built, optical-microscope-based projection lithography system and developed in MF312 diluted with deionized water (2:3 vol. ratio) for 1 min. Ti/Au (40 nm/ 60 nm) electrodes were sputter-deposited (Lesker PVD 75), and finally, the photoresist film was lifted off in warm acetone (~90 °C).

4.5 Structural and Electrical Characterization: The as-infiltrated organic-inorganic hybrids and final infiltration-synthesized inorganic nanostructures were characterized by SEM (Hitachi S-4800), TEM (JEOL 2100; 200 kV), and scanning TEM (FEI Talos F200X; 200 kV; equipped with the EDS elemental mapping capability). The cross-sectional TEM samples were prepared by the standard in-situ lift-out procedure using Ga ion milling in a focused ion beam system (FEI Helios 600 Nanolab). The two-probe I-V characteristics of ZnO nanomesh devices were measured by using an electrical probe station (Signatone) equipped with a dark box and a high-precision semiconductor parameter analyzer (Agilent). For the illuminated I-V characteristics, the devices were soaked for 3 min under the microscope tungsten light before initiating measurements.

Conflicts of interest

There are no conflicts to declare.

Acknowledgments

The research was carried out at the Center for Functional Nanomaterials (CFN), Brookhaven National Laboratory (BNL), which is supported by the US Department of Energy, Office of Basic Energy Sciences, under Contract No. DE-SC0012704. We thank Chenwei Liu for assisting the characterization of synthesized PS-*r*-P2VP samples.

Notes and references

1 Q. Peng, Y. C. Tseng, S. B. Darling and J. W. Elam, *Adv. Mater.*, 2010, **22**, 5129-5133.
2 Q. Peng, Y. C. Tseng, S. B. Darling and J. W. Elam, *ACS Nano*, 2011, **5**, 4600-4606.
3 X. Ye, J. Kestell, K. Kisslinger, M. Liu, R. B. Grubbs, J. A. Boscoboinik and C.-Y. Nam, *Chem. Mater.*, 2017, **29**, 4535-4545.
4 J. Kamcev, D. S. Germack, D. Nykypanchuk, R. B. Grubbs, C. Y. Nam and C. T. Black, *ACS Nano*, 2013, **7**, 339-346.
5 Y.-C. Tseng, Q. Peng, L. E. Ocola, D. A. Czaplewski, J. W. Elam and S. B. Darling, *J. Vac. Sci. Technol., B: Nanotechnol. Microelectron.: Mater., Process., Meas., Phenom.*, 2011, **29**, 1-4.
6 Y. C. Tseng, Q. Peng, L. E. Ocola, J. W. Elam and S. B. Darling, *J. Phys. Chem. C*, 2011, **115**, 17725-17729.
7 C.-Y. Nam, A. Stein, K. Kisslinger and C. T. Black, *Appl. Phys. Lett.*, 2015, **107**, 1-4.
8 Y. C. Tseng, A. U. Mane, J. W. Elam and S. B. Darling, *Adv. Mater.*, 2012, **24**, 2608-2613.
9 C.-Y. Nam, A. Stein and K. Kisslinger, *J. Vac. Sci. Technol., B: Nanotechnol. Microelectron.: Mater., Process., Meas., Phenom.*, 2015, **33**, 1-7.
10 S. M. Lee, E. Pippel, O. Moutanabbir, I. Gunkel, T. Thurn-Albrecht and M. Knez, *ACS Appl. Mater. Interfaces*, 2010, **2**, 2436-2441.

11 S.-M. Lee, E. Pippel, U. Gösele, C. Dresbach, Y. Qin, C. V. Chandran, T. Bräuniger, G. Hause and M. Knez, *Science (New York, N.Y.)*, 2009, **324**, 488-492.
12 B. Gong, Q. Peng, J. S. Jur, C. K. Devine, K. Lee and G. N. Parsons, *Chem. Mater.*, 2011, **23**, 3476-3485.
13 B. Gong, J. C. Spagnola and G. N. Parsons, *J. Vac. Sci. Technol., A*, 2012, **30**, 1-5.
14 Y. Yu, Z. Li, Y. Wang, S. Gong and X. Wang, *Adv. Mater.*, 2015, **27**, 4938-4944.
15 Y. Yu and X. Wang, *Extreme Mechanics Letters*, 2016, **9**, 514-530.
16 M. Lorenzoni, L. Evangelio, M. Fernández-Regúlez, C. Nicolet, C. Navarro and F. Pérez-Murano, *J. Phys. Chem. C*, 2017, **121**, 3078-3086.
17 K. J. Dusoe, X. Ye, K. Kisslinger, A. Stein, S. W. Lee and C. Y. Nam, *Nano Lett.*, 2017, **17**, 7416-7423.
18 E. Barry, A. U. Mane, J. A. Libera, J. W. Elam and S. B. Darling, *J. Mater. Chem. A*, 2017, **5**, 2929-2935.
19 A. Checco, B. M. Ocko, A. Rahman, C. T. Black, M. Tasinkevych, A. Giacomello and S. Dietrich, *Phys. Rev. Lett.*, 2014, **112**, 1-5.
20 A. Checco, A. Rahman and C. T. Black, *Adv. Mater.*, 2014, **26**, 886-891.
21 D. Berman, S. Guha, B. Lee, J. W. Elam, S. B. Darling and E. V. Shevchenko, *ACS Nano*, 2017, **11**, 2521-2530.
22 P. Mokarian-Tabari, R. Senthamaraikannan, C. Glynn, T. W. Collins, C. Cummins, D. Nugent, C. O'Dwyer and M. A. Morris, *Nano Lett.*, 2017, **17**, 2973-2978.
23 L. E. Ocola, A. Connolly, D. J. Gosztola, R. D. Schaller and A. Yanguas-Gil, *J. Phys. Chem. C*, 2017, **121**, 1893-1903.
24 L. E. Ocola, D. J. Gosztola, A. Yanguas-Gil, H.-S. Suh and A. Connolly, San Francisco, California, United States, 2016.
25 C. Cummins, T. Ghoshal, J. D. Holmes and M. A. Morris, *Adv. Mater.*, 2016, **28**, 5586-5618.
26 C. Cummins and M. A. Morris, *Microelectron. Eng.*, 2018, **195**, 74-85.
27 R. Kothari, M. R. Beaulieu, N. R. Hendricks, S. Li and J. J. Watkins, *Chem. Mater.*, 2017, **29**, 3908-3918.
28 P. La Fata, R. Puglisi, S. Lombardo and C. Bongiorno, *Superlattices Microstruct.*, 2008, **44**, 693-698.
29 S. Krishnamoorthy, C. Hinderling and H. Heinzelmann, *Mater. Today*, 2006, **9**, 40-47.
30 M. Zhou, Y. N. Wu, B. Wu, X. Yin, N. Gao, F. Li and G. Li, *Chem Asian J*, 2017, **12**, 2044-2047.
31 H. M. Jin, D. Y. Park, S. J. Jeong, G. Y. Lee, J. Y. Kim, J. H. Mun, S. K. Cha, J. Lim, J. S. Kim, K. H. Kim, K. J. Lee and S. O. Kim, *Adv. Mater.*, 2017, **29**, 1-7.
32 C. Jin, B. C. Olsen, E. J. Luber and J. M. Buriak, *Chem. Mater.*, 2017, **29**, 176-188.
33 R. A. Segalman, *Mater. Sci. Eng. R Rep.*, 2005, **48**, 191-226.
34 A. Knoll, A. Horvat, K. S. Lyakhova, G. Krausch, G. J. A. Sevink, A. V. Zvelindovsky and R. Magerle, *Phys. Rev. Lett.*, 2002, **89**, 1-4.
35 R. A. Farrell, N. Petkov, M. T. Shaw, V. Djara, J. D. Holmes and M. A. Morris, *Macromolecules*, 2010, **43**, 8651-8655.
36 M. Witt and H. W. Roesky, *Curr. Sci.*, 2000, **78**, 410-430.
37 M. Biswas, J. A. Libera, S. B. Darling and J. W. Elam, *J. Phys. Chem. C*, 2015, **119**, 14585-14592.
38 M. Biswas, J. A. Libera and S. B. Darling, *Chem. Mater.*, 2014, **26**, 6135-6141.
39 A. Rahman, P. W. Majewski, G. Doerk, C. T. Black and K. G. Yager, *Nat. Commun.*, 2016, **7**, 1-8.
40 H. Gullapalli, V. S. Vemuru, A. Kumar, A. Botello-Mendez, R. Vajtai, M. Terrones, S. Nagarajaiah and P. M. Ajayan, *Small*, 2010, **6**, 1641-1646.
41 M. P. Lu, J. Song, M. Y. Lu, M. T. Chen, Y. Gao, L. J. Chen and Z. L. Wang, *Nano Lett.*, 2009, **9**, 1223-1227.
42 Y. Zhang, S. Zhuang, X. Xu and J. Hu, *Opt. Mater.*, 2013, **36**, 169-172.
43 L. F. Dong, Z. L. Cui and Z. K. Zhang, *Nanostruct. Mater.*, 1997, **8**, 815-823.
44 C. Y. Nam, A. Stein, K. Kisslinger and C. T. Black, *Appl. Phys. Lett.*, 2015, **107**, 1-4.
45 Q. Yang, X. Guo, W. Wang, Y. Zhang, S. Xu, D. H. Lien and Z. L. Wang, *ACS Nano*, 2010, **4**, 6285-6291.
46 H. J. Fan, W. Lee, R. Hauschild, M. Alexe, G. Le Rhun, R. Scholz, A. Dadgar, K. Nielsch, H. Kalt, A. Krost, M. Zacharias and U. Gosele, *Small*, 2006, **2**, 561-568.
47 Y. Lai, M. Meng, Y. Yu, X. Wang and T. Ding, *Appl. Catal., B*, 2011, **105**, 335-345.
48 C. Y. Nam and A. Stein, *Adv. Opt. Mater.*, 2017, **5**, 1-11.
49 Y. She, J. Lee, B. T. Diroll, T. W. Scharf, E. V. Shevchenko and D. Berman, *Nanotechnology*, 2018, **29**, 1-10.
50 Y. She, J. Lee, B. Lee, B. T. Diroll, T. Scharf, E. V. Shevchenko and D. Berman, *Langmuir*, 2019, **35**, 796-803.
51 B. Nasr, S. Dasgupta, D. Wang, N. Mechau, R. Kruk and H. Hahn, *J. Appl. Phys.*, 2010, **108**, 1-6.
52 C. Cummins, A. P. Bell and M. A. Morris, *Nanomaterials (Basel)*, 2017, **7**, 1-12.
53 P. W. Majewski, A. Rahman, C. T. Black and K. G. Yager, *Nat. Commun.*, 2015, **6**, 1-6.
54 J. Chai, D. Wang, X. Fan and J. M. Buriak, *Nat. Nanotechnol.*, 2007, **2**, 500-506.
55 C. Cummins, A. Gangnaik, R. A. Kelly, A. J. Hydes, J. O'Connell, N. Petkov, Y. M. Georgiev, D. Borah, J. D. Holmes and M. A. Morris, *Chem. Mater.*, 2015, **27**, 6091-6096.
56 S. Ji, C.-C. Liu, J. G. Son, K. Gotrik, G. S. W. Craig, P. Gopalan, F. J. Himpsel, K. Char and P. F. Nealey, *Macromolecules*, 2008, **41**, 9098-9103.
57 M. Aizawa and J. M. Buriak, *J. Am. Chem. Soc.*, 2006, **128**, 5877-5886.
58 J. P. Spatz, V. Z. H. Chan, S. Mößmer, F. M. Kamm, A. Plettl, P. Ziemann and M. Möller, *Adv. Mater.*, 2002, **14**, 1827-1832.
59 J. I. Abes, R. E. Cohen and C. A. Ross, *Chem. Mater.*, 2003, **15**, 1125-1131.
60 J. P. Spatz, S. Mößmer and M. Möller, *Chem. Eur. J.*, 1996, **2**, 1552-1555.
61 A. Horechyy, N. E. Zafeiropoulos, B. Nandan, P. Formanek, F. Simon, A. Kiriy and M. Stamm, *J. Mater. Chem.*, 2010, **20**, 7734-7741.
62 O. El-Atwani, T. Aytun, O. F. Mutaf, V. Srot, P. A. van Aken and C. W. Ow-Yang, *Langmuir*, 2010, **26**, 7431-7436.
63 S. Cao, G. Gody, W. Zhao, S. Perrier, X. Peng, C. Ducati, D. Zhao and A. K. Cheetham, *Chem. Sci.*, 2013, **4**, 3573-3577.
64 C. Cummins, D. Borah, S. Rasappa, A. Chaudhari, T. Ghoshal, B. M. D. O'Driscoll, P. Carolan, N. Petkov, J. D. Holmes and M. A. Morris, *J. Mater. Chem. C*, 2013, **1**, 7841-7951.
65 T. Ghoshal, A. Chaudhari, C. Cummins, M. T. Shaw, J. D. Holmes and M. A. Morris, *Soft Matter*, 2016, **12**, 5429-5437.
66 C. Cummins, A. Gangnaik, R. A. Kelly, D. Borah, J. O'Connell, N. Petkov, Y. M. Georgiev, J. D. Holmes and M. A. Morris, *Nanoscale*, 2015, **7**, 6712-6721.
67 C. Cummins, R. A. Kelly, A. Gangnaik, Y. M. Georgiev, N. Petkov,

J. D. Holmes and M. A. Morris, *Macromol. Rapid Commun.*, 2015, **36**, 762-767.
68 V. Suresh, M. S. Huang, M. P. Srinivasan and S. Krishnamoorthy, *ACS Appl. Mater. Interfaces*, 2013, **5**, 5727-5732.
69 S. Xiong, L. Wan, Y. Ishida, Y.-A. Chapuis, G. S. W. Craig, R. Ruiz and P. F. Nealey, *ACS Nano*, 2016, **10**, 7855-7865.
70 H. I. Akyildiz, M. Lo, E. Dillon, A. T. Roberts, H. O. Everitt and J. S. Jur, *J. Mater. Res.*, 2014, **29**, 2817-2826.
71 H. I. Akyildiz, R. P. Padbury, G. N. Parsons and J. S. Jur, *Langmuir*, 2012, **28**, 15697-15704.
72 K. Manandhar, J. A. Wollmershauser, J. E. Boercker and B. N. Feigelson, *Journal of Vacuum Science & Technology A: Vacuum, Surfaces, and Films*, 2016, **34**, 1-9.
73 J. M. Lownsbury, J. A. Gladden, C. T. Campbell, I. S. Kim and A. B. F. Martinson, *Chem. Mater.*, 2017, **29**, 8566-8577.
74 X. Li, N. C. Fan and H. J. Fan, *Chem. Vap. Deposition*, 2013, **19**, 104-110.
75 A. I. Aria, K. Nakanishi, L. Xiao, P. Braeuninger-Weimer, A. A. Sagade, J. A. Alexander-Webber and S. Hofmann, *ACS Appl Mater Interfaces*, 2016, **8**, 30564-30575.
76 S. W. K. B. B. Burton, S. W. Rhee and S. M. George, *J. Phys. Chem. C*, 2009, **113**, 8249–8257.
77 I. P. Oliveri, G. Maccarrone and S. Di Bella, *J. Org. Chem.*, 2011, **76**, 8879-8884.
78 E. C. Dandley, C. D. Needham, P. S. Williams, A. H. Brozena, C. J. Oldham and G. N. Parsons, *J. Mater. Chem. C*, 2014, **2**, 9416-9424.
79 M. Biswas, J. A. Libera and S. B. Darling, *Chem. Mater.*, 2014, **26**, 6135-6141.
80 D. R. Stull, *Ind. Eng. Chem.*, 1947, **39**, 517-540.
81 C. Travis and R. Adomaitis, *Processes*, 2013, **1**, 128-152.
82 T. Keuter, N. H. Menzler, G. Mauer, F. Vondahlen, R. Vaßen and H. P. Buchkremer, *J. Vac. Sci. Technol., A*, 2015, **33**, 1-7.
83 A. Tavakkoli K. G, S. M. Nicaise, K. R. Gadelrab, A. Alexander-Katz, C. A. Ross and K. K. Berggren, *Nature Communications*, 2016, **7**, 1-10.
84 C. L. Carpenter, S. Nicaise, P. L. Theofanis, D. Shykind, K. K. Berggren, K. T. Delaney and G. H. Fredrickson, *Macromolecules*, 2017, **50**, 8258-8266.
85 H. C. Kim, C. T. Rettner and L. Sundström, *Nanotechnology*, 2008, **19**, 1-6.
86 G. T. Pickett, T. A. Witten and S. R. Nagel, *Macromolecules*, 1993, **26**, 3194-3199.
87 S.-M. Park, B. C. Berry, E. Dobisz and H.-C. Kim, *Soft Matter*, 2009, **5**, 957-961.
88 X. Man, P. Zhou, J. Tang, D. Yan and D. Andelman, *Macromolecules*, 2016, **49**, 8241-8248.
89 E. Han, H. Kang, C. C. Liu, P. F. Nealey and P. Gopalan, *Adv. Mater.*, 2010, **22**, 4325-4329.
90 J. Wu, Y. Zhao, C. Z. Zhao, L. Yang, Q. Lu, Q. Zhang, J. Smith and Y. Zhao, *Materials*, 2016, **9**, 1-10.
91 O. Nennewitz, H. Schmidt, J. Pezoldt, T. Stauden, J. Schawohl and L. Spiess, *Phys. Status Solidi A*, 1994, **145**, 283-288.
92 Y. C. Lee, S. Y. Hu, W. Water, K. K. Tiong, Z. C. Feng, Y. T. Chen, J. C. Huang, J. W. Lee, C. C. Huang, J. L. Shen and M. H. Cheng, *J. Lumin.*, 2009, **129**, 148-152.
93 A. Janotti and C. G. Van de Walle, *Rep. Prog. Phys.*, 2009, **72,** 1-29.
94 Y. R. Jang, K.-H. Yoo and S. M. Park, *J. Vac. Sci. Technol., A*, 2010, **28**, 216-219.
95 H. Morkoç and Ü. Özgur, in *Zinc Oxide: Fundamentals, Materials and Device Technology*, WILEY-VCH Verlag GmbH & Co. KGaA, Weinheim, 2009, ch. 1, pp. 1-76.
96 L. Yao, W. Pan, J. Luo, X. Zhao, J. Cheng and H. Nishijima, *Nano Lett.*, 2018, **18**, 130-136.
97 P. Banerjee, W.-J. Lee, K.-R. Bae, S. B. Lee and G. W. Rubloff, *J. Appl. Phys.*, 2010, **108**, 1-7.
98 A. T. Güntner, N. J. Pineau, D. Chie, F. Krumeich and S. E. Pratsinis, *J. Mater. Chem. B*, 2016, **4**, 5358-5366.
99 S. Suwanboon, P. Amornpitoksuk and A. Sukolrat, *Ceram. Int.*, 2011, **37**, 1359-1365.
100 M. Naeem, S. Qaseem, I. H. Gul and A. Maqsood, *J. Appl. Phys.*, 2010, **107**, 1-7.
101 I. Todd, in *Nanoscale Science and Technology*, ed. I. W. H. a. M. G. Robert W. Kelsal, John Wiley & Sons Ltd, West Sussex, England 2005, ch. 5, pp. 237-281.
102 B. D. Cullity, in *Elements of DIffraction* Addison-Wesley Publishing Company, Inc., United States of America, Second edn., 1978, ch. 3, pp. 95-103.
103 D. J. Lee, K. J. Kim, S. H. Kim, J. Y. Kwon, J. Xu and K. B. Kim, *J. Mater. Chem. C*, 2013, **1**, 4761-4769.
104 Q. Shao, C. Wang, J. A. Zapien, C. W. Leung and A. Ruotolo, *J. Appl. Phys.*, 2015, **117**, 1-4.
105 F. Du, R. C. Scogna, W. Zhou, S. Brand, J. E. Fischer and K. I. Winey, *Macromolecules*, 2004, **37**, 9048-9055.
106 K. M. Diederichsen, R. R. Brow and M. P. Stoykovich, *ACS Nano*, 2015, **9**, 2465-2476.
107 I. P. Campbell, G. J. Lau, J. L. Feaver and M. P. Stoykovich, *Macromolecules*, 2012, **45**, 1587-1594.
108 I. P. Campbell, C. He and M. P. Stoykovich, *ACS Macro Lett.*, 2013, **2**, 918-923.
109 C. Soci, A. Zhang, B. Xiang, S. A. Dayeh, D. P. Aplin, J. Park, X. Y. Bao, Y. H. Lo and D. Wang, *Nano Lett*, 2007, **7**, 1003-1009.
110 C.-Y. Tsay, H.-C. Cheng, C.-Y. Chen, K.-J. Yang and C.-K. Lin, *Thin Solid Films*, 2009, **518**, 1603-1606.

ToC Figure

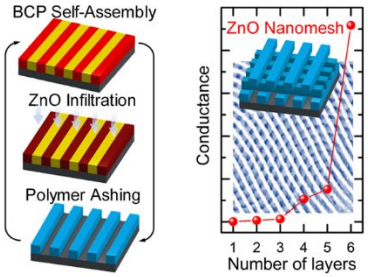

Optoelectrically functional 3D ZnO nanomeshes are synthesized via vapor-phase material infiltration into hierarchically self-assembled block copolymer thin films.